Layered Lepidocrocite Type Structure Isolated by Revisiting the Sol–Gel Chemistry of Anatase TiO 2 : A New Anode Material for Batteries

Jiwei Ma, Kyle G Reeves, Ana-Gabriela Porras Gutierrez, Monique Body, Christophe Legein, Katsuyoshi Kakinuma, Olaf Borkiewicz, Karena W Chapman, Henri Groult, Mathieu Salanne, et al.

Article

Layered Lepidocrocite Type Structure Isolated by Revisiting the Sol-Gel Chemistry of Anatase TiO2: a New Anode Material for Batteries

Jiwei Ma, Kyle G. Reeves, Ana-Gabriela Porras Gutierrez, Monique Body, Christophe Legein, Katsuyoshi Kakinuma, Olaf J. Borkiewicz, Karena W Chapman, Henri Groult, Mathieu Salanne, and Damien Dambournet

Chem. Mater., **Just Accepted Manuscript** • DOI: 10.1021/acs.chemmater.7b02674 • Publication Date (Web): 07 Sep 2017

Layered Lepidocrocite Type Structure Isolated by Revisiting the Sol-Gel Chemistry of Anatase TiO_2: a New Anode Material for Batteries

Jiwei Ma,*[,†] Kyle G. Reeves,[†] Ana-Gabriela Porras Gutierrez,[†] Monique Body,[‡] Christophe Legein,[‡] Katsuyoshi Kakinuma,[§] Olaf J. Borkiewicz,[∥] Karena W. Chapman,[∥] Henri Groult,[†] Mathieu Salanne,[†,⊥] and Damien Dambournet*[,†,⊥]

[†]Sorbonne Universités, UPMC Univ Paris 06, CNRS, UMR 8234, PHENIX, 4 Place Jussieu, 75005 Paris, France

[‡]Université Bretagne Loire, Université du Maine, UMR CNRS 6283, Institut des Molécules et des Matériaux du Mans (IMMM), Avenue Olivier Messiaen, 72085 Le Mans Cedex 9, France

[§]Fuel Cell Nanomaterials Center, University of Yamanashi, 6-43 Miyamae-cho, Kofu 400-0021, Yamanashi, Japan

[∥]X-ray Science Division, Advanced Photon Source, Argonne National Laboratory, Argonne, Illinois 60439, USA

[⊥]Réseau sur le Stockage Electrochimique de l'Energie (RS2E), FR CNRS 3459, 80039 Amiens, France

ABSTRACT: Searches for new electrode materials for batteries must comply on financial and environmental costs to be useful in practical devices. The sol-gel chemistry has been widely used to design and implemented new concepts for the emergence of advanced materials such as hydride organic-inorganic composites. Here, we show that the simple reaction system including titanium alkoxide and water can be used to stabilize a new class of electrode materials. By investigating the crystallization path of anatase TiO_2, an X-ray amorphous intermediate phase has been identified whose local structure probed by the pair distribution function, ^{1}H solid-state NMR and DFT calculations, consists of a layered-type structure as found in the lepidocrocite. This phase presents the following general formula $Ti_{2-x}\square_xO_{4-4x}(OH)_{4x}.nH_2O$ ($x \sim 0.5$) where the substitution of oxide by hydroxide anions leads to the formation of titanium vacancies ($\square$) and H_2O molecules are located in interlayers. Solid-state ^{1}H NMR has enabled to characterize three main hydroxide environments that are Ti$\square$-OH, $Ti_2\square_2$-OH and $Ti_3\square$-OH and layered H_2O molecules. The electrochemical properties of this phase were further investigated versus lithium and is shown to be very promising with reversible capacities of around 200 mAh.g^{-1} and an operating voltage of 1.55 V. We further showed that the lithium intercalation proceeds via a solid-solution mechanism. ^{7}Li solid-state NMR and DFT calculations allowed to identify lithium host sites that are located at the titanium vacancies and interlayer space with lithium being solvated by structural water molecules. The easy fabrication, the absence of lithium and easier recycling and the encouraging properties makes this class of materials very attractive for competitive electrodes for batteries. We thus demonstrate that the revisit of an "old" chemistry with advanced characterization tools allows discovering new materials of technological relevance.

INTRODUCTION

The development of electrical energy storage devices such as lithium-ion batteries (LIBs) reflects the growing energy demand related to multiple applications spanning the electrification of transports, grid storage to electronics.[1] The success in new technologies relies on the ability to meet key criteria such as cost and sustainability.[2] In this scope, Larcher and Tarascon[2] rationalized the total cost, *i.e.* financial and environmental, associated with building a lithium cell by considering four factors that are the chemical composition (elemental abundance and cost), synthesis processes, implementation in the system (electrode processing) and recycling (elements recovery or reuses).

Commercialized negative electrodes for LIBs are currently dominated by carbonaceous-based and Ti-based materials. Although natural graphite is considered to be cheaper and more sustainable than the synthetic counterpart, it requires a purification step using thermal or chemical treatments to be electrochemically active.[3] These steps contribute to both financial and environmental costs which incite toward the use of greener materials.

The development of higher voltage anode materials such as $Li_4Ti_5O_{12}$ (LTO) has emerged due to safety concerns encountered with some carboneous-based electrodes.[4] Particularly more adapted for high-power applications, LTO is, however, typically prepared via a solid state reaction between TiO_2 and a lithium salt at high temperature (T> 600 °C) leading again to financial and environmental costs. Moreover, lithium atoms enable to stabilize the spinel type structure but are not electrochemically active (as opposed to the cathode that serves as the lithium reservoir) and make recycling more complicated. Finally, LTO offers a limited capacity. Hence, the search for new electrodes materials needs to comply on sustainability, scalability, cost, easier recycling and high performances. In this scope, we re-investigated the sol-gel chemistry of Ti-oxide and identify an amorphous intermediate to anatase TiO_2 featuring a layered like structure enabling reversible lithium uptake and release with capacity higher than LTO.

EXPERIMENTAL

Synthesis protocol.

A solution containing 0.81 mL of ultrapure water and 25.19 mL of isopropanol (Sigma-Aldrich) was added to 4 mL of titanium isopropoxide (Sigma-Aldrich) in a 45 mL Teflon line container.

After sealing, the solution was heated at the fixed temperature, *i.e.* 90, 100 and to 110 °C, for 12 hours. After cooling to room temperature, the white powder was recovered from the solution using centrifugation and washed several times with ethanol. The solid was dried at 80 °C overnight, and further outgassed at 100 °C for 2 hours prior to electrochemical characterizations.

Chemical Lithiation.

Chemical lithiation was carried out by using the intercalating agent n-butyl lithium (Sigma-Aldrich, 1.6 M in hexanes).[5] Briefly, $Ti_{1.5}\square_{0.5}O_2(OH)_2.0.55H_2O$ powder was firstly dispersed into the hexanes, after which an excess n-butyl lithium was slowly added while stirring the mixture with a fixed Li/Ti molar ratio of 0.5, 1.1 and 2.2, respectively. The mixture was stirred for 48 hours at room temperature. Lithiation of $Ti_{1.5}\square_{0.5}O_2(OH)_2.0.55H_2O$ produced a color change from white to dark grey over several hours, and with a final color change to yellow. After reaction, the products were washed several times with hexanes and dried under vacuum. All subsequent operations were carried out in an argon-filled glove box. Lithium contents of lithiated samples were determined using a Varian 715-ES inductively coupled plasma (ICP) analysis system with atomic emission spectroscopy detection (AES).

Physical Characterization.

Powder X-ray diffraction (XRD) data were collected using a Rigaku diffractometer, equipped with Cu Kα radiation, in a Bragg −Brentano geometry.

The thermogravimetric analysis (TGA) was performed with a METTLER TOLEDO thermogravimetric analyzer. Samples were heated from room temperature to 600 °C under argon atmosphere at a heating rate of 5 °C.min^{-1}.

Scanning Transmission Electron Microscopy (STEM) measurements were performed with a Hitachi, HD-2700 STEM. An aberration-corrected STEM equipped with a cold field-emission electron source, operating with a probe current of 10 µA at 200 kV accelerating voltage was used. Transmission Electron Microscopy (TEM) analysis was performed using a JEOL 2010 UHR microscope operating at 200 kV equipped with a TCD camera.

Synchrotron diffraction data were collected at the 11-ID-B beamline at the Advanced Photon Source at Argonne National Laboratory, using high energy X-rays (λ = 0.2128 Å) allowing high values of momentum transfer.[6,7] One-dimensional diffraction data were obtained by integrating the raw 2D total scattering data in Fit2D.[8] PDFs, G(r), were extracted from the background and Compton scattering corrected data following Fourier transformation using PDFgetX2.[9] The PDFs were subsequently modelled using PDFgui.[10]

^{1}H and ^{7}Li solid-state NMR spectroscopy.

^{1}H and ^{7}Li solid-state magic angle spinning (MAS) NMR experiments were performed on a Bruker Avance 300 spectrometer operating at 7.0 T (^{1}H and ^{7}Li Larmor frequencies of 300.2 and 116.7 MHz, respectively), using a 1.3 mm and 2.5 mm CP-MAS probe head, respectively. The room temperature ^{1}H MAS spectra were recorded using a Hahn echo sequence with an interpulse delay equal to one rotor period. The 90° pulse length was set to 1.25 µs and the recycle delay was set to 5 s. The room temperature ^{7}Li MAS spectra were recorded using a single pulse sequence. The 90° pulse length was set to 0.8 µs and the recycle delay was set to 20 s. ^{1}H and ^{7}Li spectra are referenced to TMS and 1 M LiCl aqueous solution, respectively and they were fitted by using the DMFit software.[11] A saturation recovery pulse sequence was employed for T_1 measurements.

Electrochemical Characterization.

Electrochemical measurements were carried out with CR2032-type coin cells. The composition of the electrode was 80 wt.% active materials, 10 wt.% Super P, and 10 wt.% polyvinylidene difluoride (PVDF) or 10 wt% sodium alginate. Copper was used as the current collector. The electrolytes were 1 M $LiPF_6$ dissolved in a mixture of ethylene carbonate (EC) and dimethyl carbonate (DMC) (1:1, v/v), 1 M $LiClO_4$ dissolved in a mixture of ethylene carbonate (EC) and dimethyl carbonate (DMC) (1:1, v/v), and 1 M $LiClO_4$ dissolved in a mixture of propylene carbonate (PC), dimethoxyethane (DME) and tetrahydrofuran (THF) (40/15/45, v/v/v). The cells were assembled with lithium metal as the anode and were tested in the voltage range of 3.0–1.0 V *vs.* Li^+/Li at different current densities.

Electronic Structure Calculations.

Density functional theory (DFT) calculations were performed using the CP2K software.[12] The GGA PBE exchange-correlation functional[13] was used along with the DZVP-MOLOPT-SR-GTH basis set. Goedecker-Teter-Hutter pseudopotentials[14] were used to describe core electrons. Ti atoms were represented explicitly using $3s^23p^63d^24s^2$ electronic orbitals and O atoms were represented using $2s^22p^4$ electronic orbitals. Calculations were performed via the Quickstep algorithm[15] as implemented in CP2K on a 4×4×1 lepidocrocite supercell (64 TiO_2 units). Given the size of the system, only the Γ-point was used to sample k-space. Periodic boundary conditions were used for all calculations. We used a plane wave cutoff of 400 Ry for all electronic structure calculations. The structure for the lepidocrocite titanate was taken from previous experimental work[16] where the spacing of basal planes of the lepidocrocite was determined to be 11.5Å.

RESULTS AND DISCUSSION

Synthesis process.

The used reaction system comprises titanium isopropoxide dissolved in isopropanol and water as a hydrolysis agent with a fixed H_2O/Ti molar ratio set to 3.33. Precipitation was obtained by thermal activation under solvothermal conditions at three different temperatures, *i.e.* 90, 100 and 110 °C, for 12 hours. **Figure 1** shows the powder X-ray diffraction patterns of the samples obtained at these temperatures. At T = 90 °C, the XRD pattern features diffuse scattered intensities with the absence of Bragg peaks characteristic of amorphous compounds. At T > 90 °C, the appearance of Bragg peaks indicates that crystallization starts to occur with peaks indexation relative to a tetragonal symmetry characteristic of anatase TiO_2. At T = 110 °C, the diffuse scattered intensities vanished suggesting that full crystallization occurred.

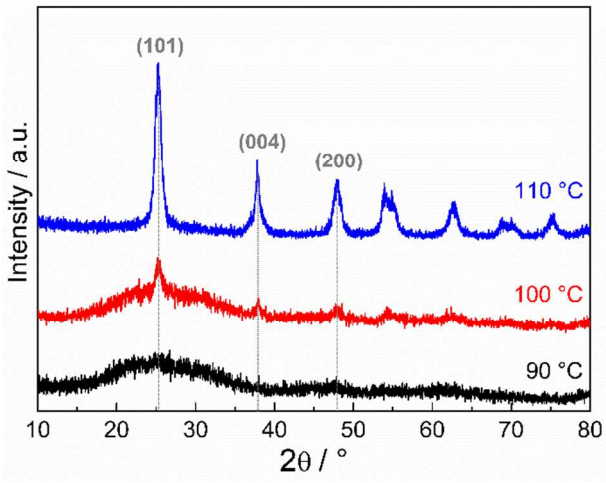

Figure 1. X-ray diffraction patterns of the samples prepared at different temperatures.

The analysis of the XRD data was further confirmed by transmission electron microscopy **(Figure 2)**. For T = 90 °C, the absence of lattice fringes confirms the amorphous state observed by XRD. At T > 90 °C, the number of crystallized particles, with

sizes of around 7 nm, growth upon increasing the reaction temperature. The measured d-spacing between lattice fringes revealed that the nanocrystals mostly expose thermodynamically stable {101} facets.[17] Assuming a truncated octahedral, *i.e.*, built from eight {101} and two {001} facets,[18] the percentages of exposed {101} and {001} facets determined by XRD are 92 and 8 %, respectively. The stabilization of the thermodynamically stable crystal shape is in good agreement with the absence of any structure directing agent during the synthesis process.[19]

The narrow temperature range in which crystallization occurs suggests that the amorphous compound prepared at 90 °C presents structural features that are closely related to anatase. Literature data on the structural analysis of amorphous "TiO_2" points toward the existence of several atomic arrangement depending on the synthesis conditions. Zhang *et al.*[20] concluded on particles built from an anatase-like crystalline core with highly distorted shell. Similarly, Fernandez-Garcia *et al.*,[21] identified a local structure related to the anatase with under-coordinated Ti cations. Borghols *et al.*,[22] suggested that the local ordering of amorphous TiO_2 is similar to anatase. Iversen *et al.*,[23] described their amorphous compound as being a titanium oxy-hydroxide with an arrangement related to anatase. Gateshki *et al.*,[24] concluded on a local structure that is closely related to the lepidocrocite-type structure.

To investigate the structural features of the amorphous intermediate, we used high-energy synchrotron-based total scattering measurements and acquired data from which the pair distribution function (PDF) was obtained for the samples prepared at different temperatures. The PDF can be defined as a histogram of all the atom-atom distances obtained by Fourier transform of total scattering data (both diffuse and Bragg) and is therefore perfectly suited for characterizating amorphous/nanostructured materials.[25] The PDF of the amorphous intermediate shows no correlations beyond 10 Å in agreement with the absence of long-range order **(Figure 3)**. We attempted to describe the local structure by refinement against two different structural models based on the anatase and lepidocrocite type structures **(Figure 3)**. These two structures are structurally related.[26] The tetragonal structure of anatase (space group $I4_1/amd$) consists of a tri-dimensional arrangement of TiO_6 octahedra linked through an edge-sharing configuration where O^{2-} is three-fold coordinated to Ti^{4+} ions. The lepidocrocite structure (space group Cmcm) displays a lamellar arrangement of TiO_6 octahedra similar to the zig-zag configuration observed in anatase. Nevertheless, it contains two inequivalent O^{2-} sites of same multiplicity that are 2-fold and 4-fold coordinated to Ti^{4+} cations

The refinement against the data using the tetragonal symmetry **(Figure 3a)** of anatase failed in reproducing the PDF features. Using the lepidocrocite like structure (space group Immm),[27] a significant improvement of the fit was obtained with most of the peaks being reproduced (**Figure 3b**).

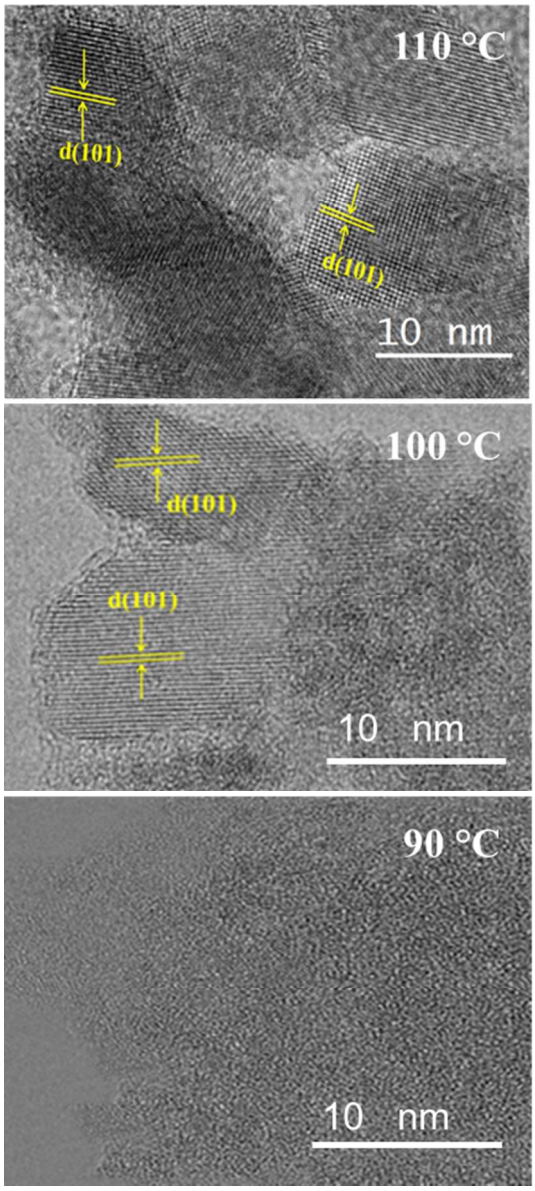

Figure 2. Transmission electron micrographs obtained on samples prepared at different temperatures.

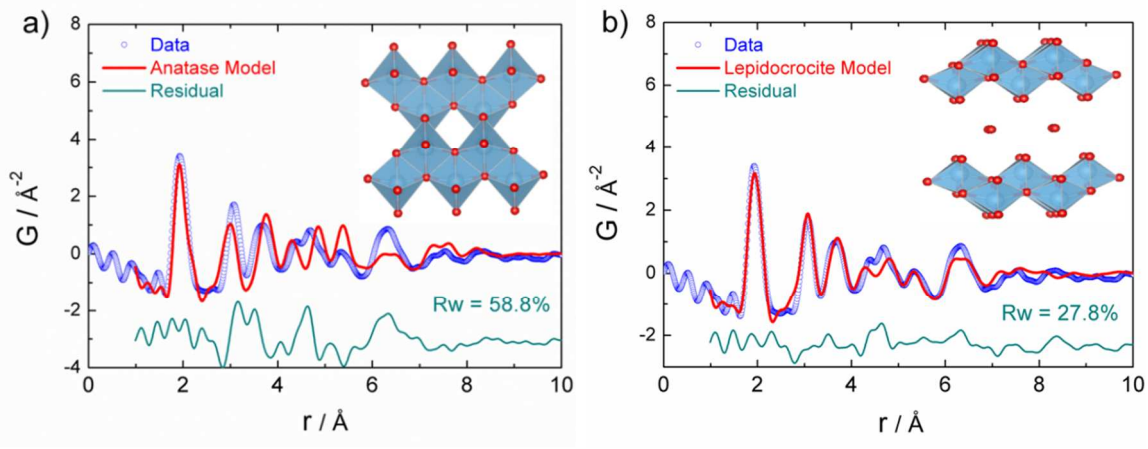

Figure 3. PDF refinements of the amorphous intermediate prepared at 90 °C using a) the anatase and b) the lepidocrocite as structural models (see insets).

Thermogravimetric analysis was used to assess the chemical composition of the amorphous phase. The TG curve **(Figure 4)** shows three steps of weight loss assigned to the departure of physisorbed water (25-100 °C), structural water (100-200 °C) and OH groups (T > 200 °C). Thermal analysis clearly indicates that the amorphous compound features an oxy-hydroxyl hydrate composition. Using the following general chemical formula $Ti_{2-x}\square_xO_{4-4x}(OH)_{4x}.nH_2O$, where the substitution of oxide by hydroxide anions leads to the formation of titanium vacancies (□) and H_2O molecules are located in interlayer, the following composition $Ti_{1.5}\square_{0.5}O_2(OH)_2.0.55H_2O$ was established (within the experimental margin error). We noted that the general composition $Ti_{2-x}\square_xO_{4-4x}(OH)_{4x}.nH_2O$ differs from the one previously proposed by Sasaki *et al.*,[15] that is $H_xTi_{2-x/4}\square_{x/4}O_4.H_2O$ featuring exchangeable protons in the form of H_3O^+.

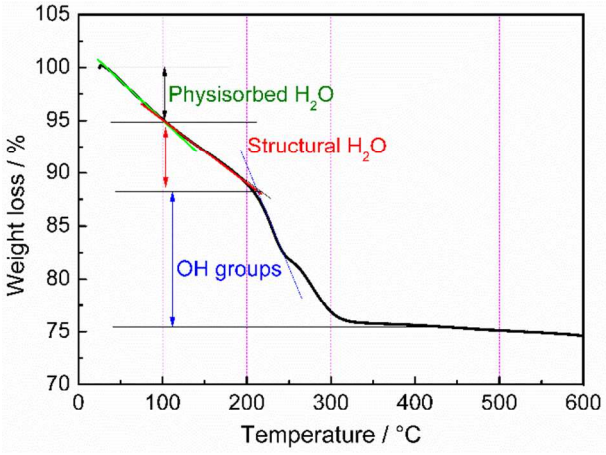

Figure 4. Thermogravimetric curve obtained on the amorphous compound ($T_{synthesis}$ = 90 °C).

The presence of both oxide and hydroxide in the vicinity of Ti^{4+} was evidenced by the inter-atomic distances observed in the first peak of the PDF of $Ti_{1.5}\square_{0.5}O_2(OH)_2.0.55H_2O$. Gaussian fit of this peak **(Figure S1** in **Supplementary Information)** allows distinguishing two sets of distances equal to 1.890 and 2.027 Å and ascribed to Ti-O and Ti-OH inter-atomic distances, respectively. The two peak areas are similar suggesting the equiproportion of the two bonds in agreement with the established chemical formula.

^1H solid-state NMR offers a direct insight into the local environment of the hydrogen atoms in the amorphous compound $Ti_{1.5}\square_{0.5}O_2(OH)_2.0.55H_2O$ **(Figure 5)**. Its spectrum was reconstructed using nine resonances (**Table 1**). Assuming a random distribution of vacancies and Ti^{4+} on the cation sites and ruling out the possibility of non-coordinated (coordinated only to vacancies) anions, yields for the anions (X= OH^-, O^{2-}) 2-fold coordinated, to an equiprobability of occurence of Ti□-X (50%) and Ti_2-X species (50%). The same assumptions lead for the anions 4-fold coordinated, to probabilities of occurence of $Ti\square_3X$, $Ti_2\square_2$-X, $Ti_3\square$-X and Ti_4-X species equal to 5.5, 20.7, 42.2 and 31.6%, respectively.

Crocker *et al.* suggested that proton chemical shift values increase upon increasing the number of Ti surrounding OH groups as exemplified by chemical shifts equal to 2.3 and 6.7 ppm assigned to terminal and bridging OH groups in anatase, respectively.[28] The NMR resonances in the ranges 1-2 ppm and 4-5 ppm and at ~7.4 and ~9.0 ppm are therefore tentatively assigned to Ti□-OH and $Ti\square_3$-OH species, Ti_2-OH and $Ti_2\square_2$-OH species, $Ti_3\square$-OH and Ti_4-OH species, respectively (**Table 1**), in agreement with recent studies on titanium oxy-hydroxy-fluoride containing titanium vacancies.[29,30] The broad resonance located at ~6.5 ppm is assigned to the H_2O molecules. Its relative intensity (~33%) supports this assignment since based on the chemical composition, OH groups and H_2O molecules account for 65% and 35% of the proton intensity, respectively. The proportions of the OH species (**Table 1**) compared to the probabilities of occurence of these species assuming a random distribution of anions on the 2-fold and 4-fold anion sites (25% of Ti□-OH and ~3% of $Ti\square_3$-OH; 25% of Ti_2-OH and ~10% of $Ti_2\square_2$-OH; ~21% of $Ti_3\square$-OH; ~16% of Ti_4-OH) show that OH groups are preferentially located in the vicinity of titanium vacancies (reducing the repulsive charge force of facing anions). Indeed, these proportions lead to average numbers of Ti^{4+} cations around OH groups and O atoms equal to ~1.9 and ~2.6, respectively.

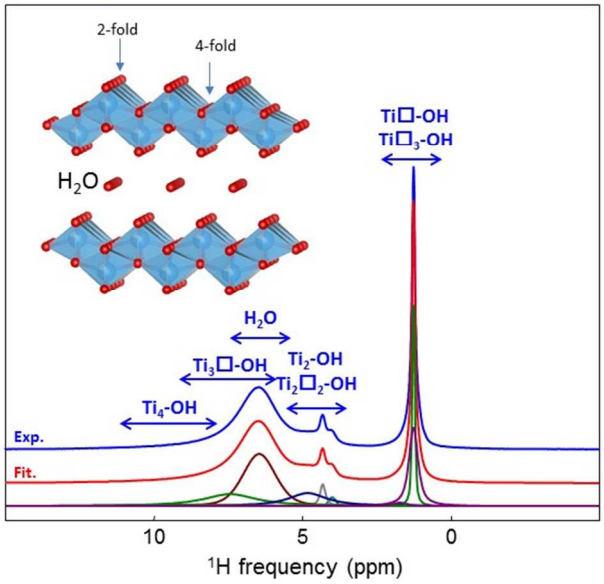

Figure 5. Experimental (blue) and fitted (red) ^1H MAS (64 kHz) NMR spectra of $Ti_{1.5}\square_{0.5}O_2(OH)_2.0.55H_2O$. The individual resonances used for the fit (see Table 1) are shown below and the assignments of these resonances are indicated. Inset: structural representation of the lepidocrocite with highlights of anions 2-fold and 4-fold coordinated to Ti^{4+} ions and layered H_2O molecules.

Table 1. Isotropic chemical shifts (δ_{iso}, ppm), line widths (LW, ppm), relative intensities (I, %), assignment of the NMR resonances used for the fit of the ^1H MAS (64 kHz) NMR spectrum of $Ti_{1.5}\square_{0.5}O_2(OH)_2.0.55H_2O$ and proportion (P_{OH}, %) of the OH species determined from the relative intensities of their NMR lines.

δ_{iso}	LW	I	Assignment	P_{OH}
1.25	0.11	11.9	Ti□-OH, $Ti\square_3$-	45.5
1.25	0.37	17.0	OH	
1.71	0.61	1.5		
3.99	0.29	1.1	Ti_2-OH, $Ti_2\square_2$-	24.1
4.31	0.22	3.0	OH	
4.82	1.6	12.0		
6.45	1.3	33.3	H_2O	
7.43	2.2	16.1	$Ti_3\square$-OH	24.1
9.03	6.6	4.2	Ti_4-OH	6.3

Crystallization mechanism.

The crystallization mechanism of the anatase phase was examined by refinements of the PDF data of the samples prepared at higher temperatures **(Figure 6)**. At T = 100°C, the crystallization of anatase starts and the data are well reproduced using a two-phases refinement including both the anatase and the amorphous lepidocrocite type phases showing that crystallization occurs via a two-phases process. At T = 110 °C, the data were refined using a single phase of anatase. Moreover, the refinement of the titanium rate occupancy indicates the presence of 12% of vacancies in the stabilized anatase phase yielding $Ti_{0.88}\square_{0.12}O_{1.52}(OH)_{0.48}$. This is supported by the ^1H MAS NMR spectrum of the sample prepared at T = 110°C (**Figure S2** in **Supplementary Information**) showing resonances assigned to $Ti\square_2$-OH, $Ti_2\square$-OH and Ti_3-OH species. Vacancies have been previously observed in sol-gel synthetized anatase $Ti_{1-x}\square_xO_{2-4x}(OH)_{4x}$ as a result from incomplete condensation of OH groups.[31] Thus, it can be postulated that the lepidocrocite is an intermediate phase prior to the crystallization of the anatase. The two-phase process can be rationalized by the following steps:

(i) Precipitation of the amorphous phase $Ti_{1.5}\square_{0.5}O_2(OH)_2.nH_2O$

(ii) Loss of structural water:

$Ti_{1.5}\square_{0.5}O_2(OH)_2.nH_2O \rightarrow Ti_{1.5}\square_{0.5}O_2(OH)_2 + n\ H_2O$

(iii) Condensation of the zig-zag chains of the lepidocrocite that re-arrange to adopt the anatase structure according to:

$Ti_{1.5}\square_{0.5}O_2(OH)_2 \rightarrow 1.705\ Ti_{0.88}\square_{0.12}O_{1.52}(OH)_{0.48} + 0.59\ H_2O$

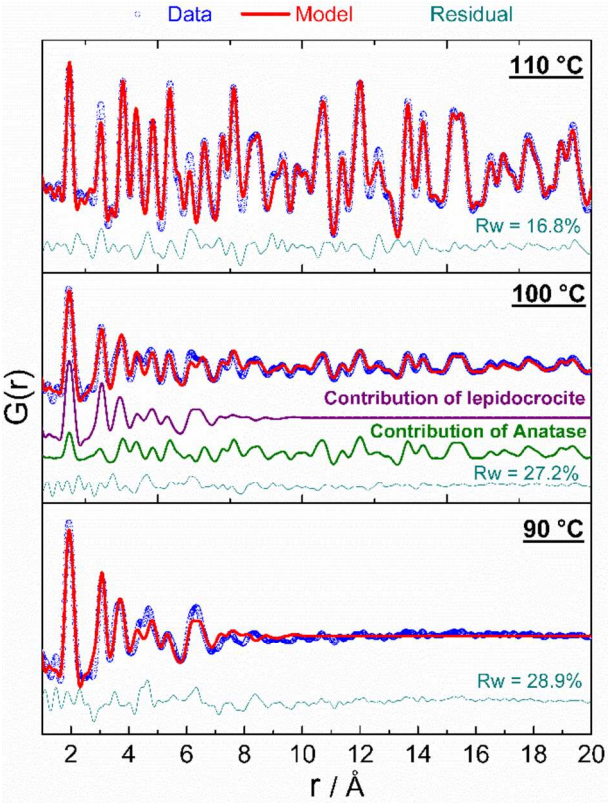

Figure 6. PDF refinements of the samples prepared at different temperatures.

Morphological aspects of the amorphous and anatase phases were investigated using scanning electron microscopy **(Figure 7)**. SEM images show that the amorphous compound consists of spherical aggregates of nano-sized particles. The anatase phase is built from larger particles with similar spherical like aggregates. The evolution of the morphology upon crystallization confirms the occurrence of the aforementioned two-phase process where the amorphous phase first precipitates and is then converted to anatase. The two-phase process thus occurs via a solid-state transformation, *i.e.*, decomposition and fusion of the intermediate amorphous particles, rather than a dissolution-recrystallization process.

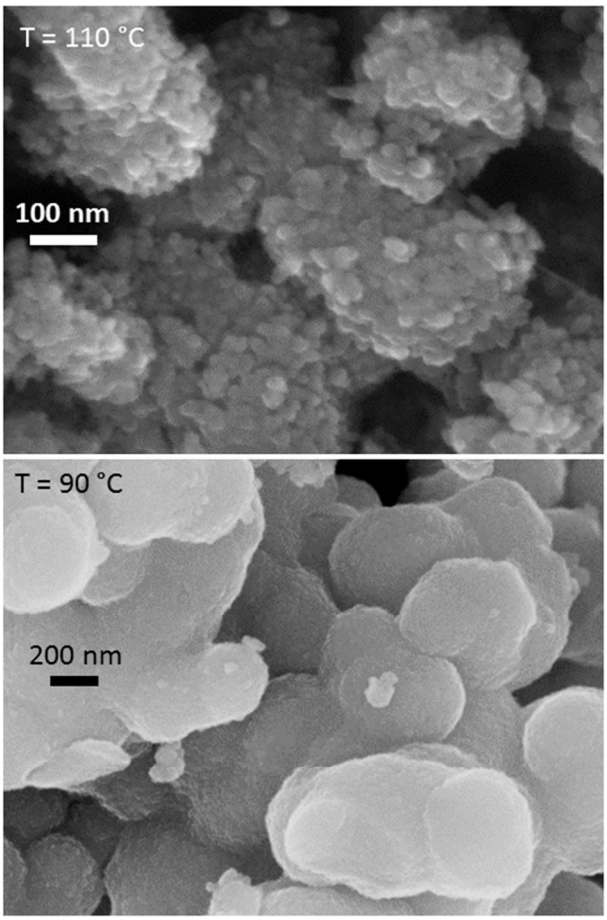

Figure 7. SEM images of the samples prepared at different temperatures.

Density Functional Theory Calculations.

Density functional theory (DFT) calculations were performed to better understand the electronic structure of the material and the chemical environments of the titanium vacancies. We first generated a 4×4×1 lepidocrocite[32] supercell ($Ti_{64}O_{128}.32H_20$) where the positions of water molecules were first approximated to be homogeneously distributed throughout the interlayer between titanate planes and were then optimized while constraining the positions of Ti and O atoms. Each titanate layer (inset Figure 5) is composed of two titanium layers (blue octahedra) and four distinct layers of oxygen atoms (red spheres). A titanium vacancy present in the titanate plane generates a void in the structure which allows for an unobstructed path between interlayers (**Figure 8a,** inset). To introduce a cationic vacancy into the lepidocrocite structure, one titanium atom from the structure was removed to generate $Ti_{63}\square_1(OH)_nO_{128-n}{\cdot}32H_2O$. In this expression, n indicates the number of oxygen atoms that were previously coordinated to the now missing titanium atom and that are hydroxylated. These oxygen atoms in the vicinity of the vacancy become three-fold and one-fold coordinated in the presence of a titanium vacancy. Mirroring the work of Grey and Wilson,[31] we systematically varied the number and positions of hydroxyl groups to determine the defect energies of a titanium vacancy. We report in **Figure 8a**

that the vacancy is likely to be most stable when the number of additional protons leads to a charge neutral vacancy (*i.e.* four OH^-). Following protonation, these oxygens are again four-fold and two-fold coordinated. A hydroxylated system with four hydroxyl groups is determined to be 429.0 meV per functional unit more stable than an identical system with no hydroxyl groups. In all cases, our calculations suggest that the lowest energy configurations are those systems in which the one-fold oxygen atoms are the preferentially protonated.

In addition to the complete passivation of the titanium vacancy, we observe a distortion to the lattice of the lepidocrocite in the vicinity of the vacancy (**Figure 8b**). The oxygen atoms immediately adjacent to the vacancy move away from the vacancy and the distances between opposite oxygen atoms in the octahedron increase by as much as 1 Å. The volume of the octahedron formed by the six surrounding oxygen atoms increases by 33.9% when the titanium atom is absent. We performed additional DFT calculations to determine the energetics of two vacancies in the lepidocrocite structure (**Supplementary Information**, **Figure S3**). These calculations suggest that titanium vacancies in the lepidocrocite structure are likely to remain far apart from one another for as long as it is structurally possible and that the distribution of vacancies and Ti^{4+} on the cation sites is not random. If the probabilities of occurrence of the $Ti_{2-x}\square_x$-X and $Ti_{4-x}\square_x$-X species calculated above are thus not accurate, this does not question the preferential location of the OH groups in the vicinity of titanium vacancies.

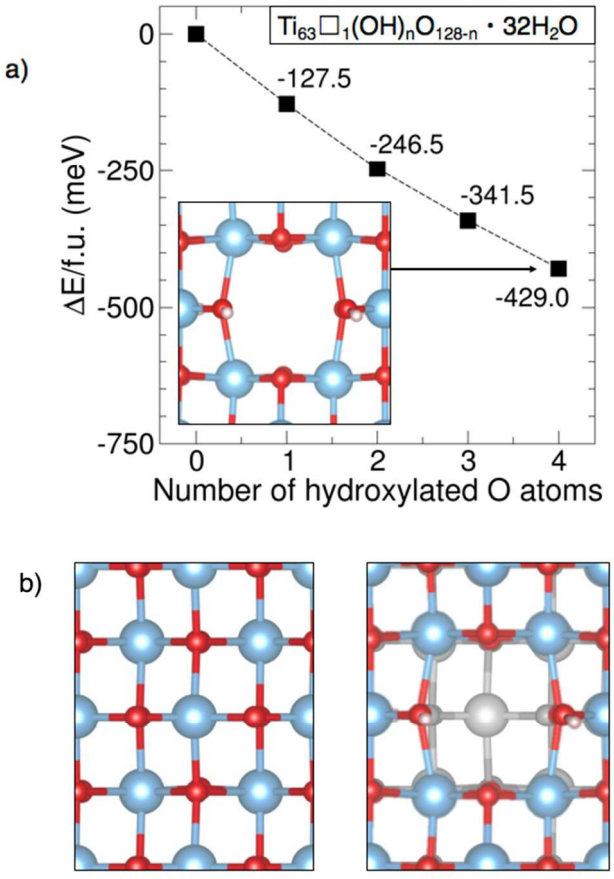

Figure 8. a) Relative energies of the lepidocrocite structure with a single vacancy as a function of the number of protons added for charge balance. Energies are reported with respect to the structure with no hydroxylation. b) The lattice on the left shows the structure of the titanate layer before the introduction of a vacancy. The lattice on the right shows the significant distortion in the vicinity of the vacancy. A superimposed image of the original structure is provided to aid in visualization.

Electrochemical properties.

The amorphous compound $Ti_{1.5}\square_{0.5}O_2(OH)_2.0.55H_2O$ was considered as a potential electrode materials for lithium-ion batteries. **Figure 9a** shows the first three discharge/charge curves obtained under galvanostatic conditions cycled against metallic lithium with 1M $LiPF_6$ in EC/DMC electrolyte and PVDF as the binder. The observed sloping curves are characteristic of the ion-intercalation of amorphous materials with minor structural changes upon redox reactions.[33] After three cycles, the charge capacity reached 207 $mAh.g^{-1}$ with an operating voltage of 1.55 V which is similar to the working potential of LTO.[4] After 50 cycles, the discharge capacity stabilized to 180 $mAh.g^{-1}$ with a 97.6 % coulombic efficiency (**Figure 9b**). Despite a gradual loss upon cycling, the reversible capacity is higher than the 150 $mAh.g^{-1}$ obtained with LTO, showing promising properties. Moreover, the calculated theoretical capacity based on the Ti^{4+}/Ti^{3+} redox couple is 270 $mAh.g^{-1}$ further highlighting potential increase in energy density as compared to LTO.

Aiming at reducing environmental cost, an alternative to PVDF binder that required the use of toxic n-methyl-2-pyrrolidone, water soluble sodium alginate was used as the binder. **Figure 9c** and **9d** show the first three discharge/charge curves and the evolution of the discharge/charge capacity upon cycling. The data are close to those obtained using PVDF demonstrating the chemical compatibility of the amorphous compound with water soluble binder.

The rate capability of the amorphous compound $Ti_{1.5}\square_{0.5}O_2(OH)_2.0.55H_2O$ was investigated at different current densities up to 600 $mA.g^{-1}$ (**Figure 10**). In the conventional electrolyte 1 M $LiPF_6$ in EC/DMC, the capacity dropped significantly upon increasing the current density with 67 $mAh.g^{-1}$ obtained under 600 $mA.g^{-1}$. Strikingly, changing the nature of the lithium salt from $LiPF_6$ to $LiClO_4$ resulted in a significant improvement of the storage capacity with around 88 $mAh.g^{-1}$ obtained under 600 $mA.g^{-1}$ showing that tailoring the solvent-solute interactions can drastically impact on the rate performance. Accordingly, we further employed a ternary mixture of PC/DME/THF with $LiClO_4$ salt (**Figure 10b**). This combination of PC/DME/THF is recognized to be a safer electrolyte when using $LiClO_4$ salt.[34] Moreover, we noticed a further capacity improvement with 114 $mAh.g^{-1}$ obtained under 600 $mA.g^{-1}$ further highlighting the key role of the solvent-solute interactions. A comparison performed with the benchmark electrode LTO showed that $Ti_{1.5}\square_{0.5}O_2(OH)_2.0.55H_2O$ exhibits higher or similar rate performances depending on the used current densities (**Supplementary Information, Figure S4**).

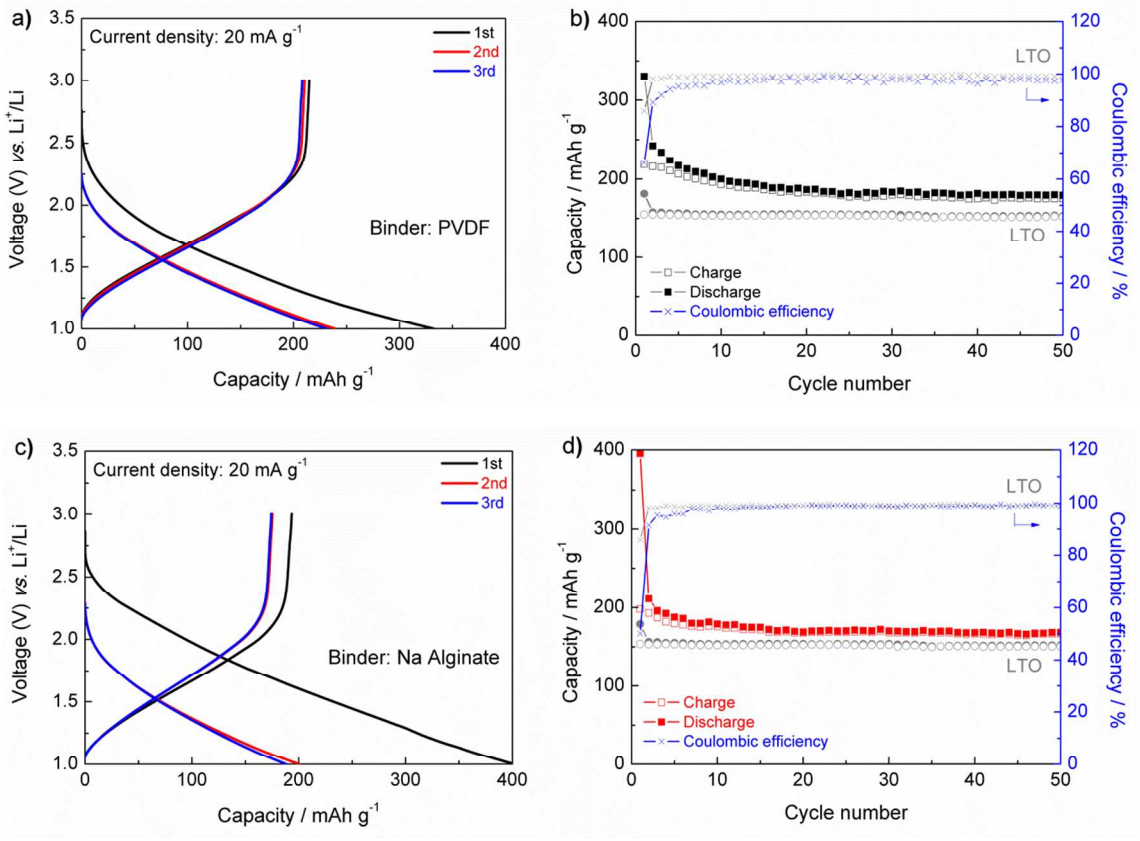

Figure 9. Galvanostatic discharge/charge curves obtained for cells cycled against metallic lithium under 20 mA.g^{-1} with 1-3 V voltage window and 1M $LiPF_6$ EC/DMC electrolyte with a) PVDF and c) sodium alginate as the binder and the corresponding cycling data b)-d).

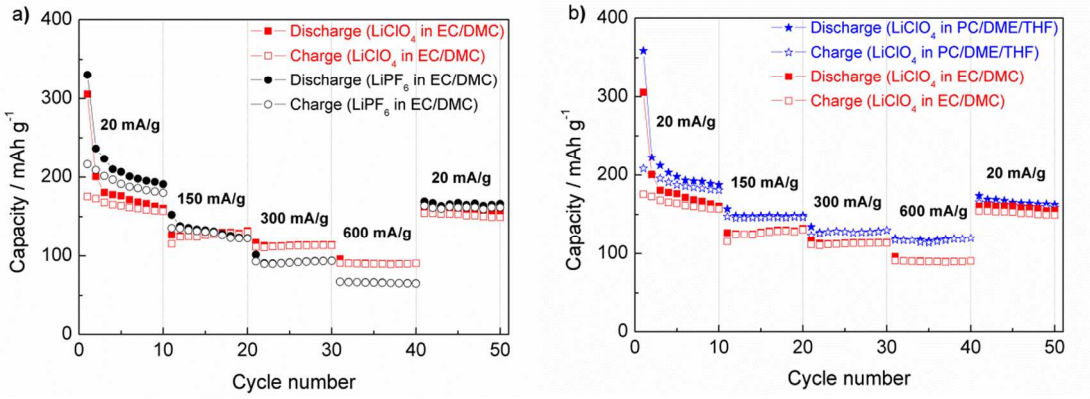

Figure 10. Rate capability obtained for cells cycled against metallic lithium under 20, 150, 300 and 600 mA.g^{-1} within the 1-3 V voltage window using (a) 1M $LiClO_4$ and 1M $LiPF_6$ in EC/DMC, and (b) 1M $LiClO_4$ in PC/DME/THF and EC/DMC.

Using 1M $LiClO_4$ in PC/DME/THF electrolyte, the cycling stability of $Ti_{1.5}\square_{0.5}O_2(OH)_2.0.55H_2O$ electrode was tested at different current densities (**Figure 11**). The cycling data show that stable capacities of 170, 150, 130 and 110 mAh g^{-1} are obtained after 50 cycles under 20, 150, 300 and 600 mA g^{-1}, respectively, showing promising results.

The electrochemical kinetics for Li ion diffusion within the layered like structure were examined by extracting the Li diffusion coefficient as a function of the depth of discharge using the galvanostatic intermittent titration technique (GITT), according to the following equation[35]:

$$D_{Li^+} = \frac{4}{\tau\pi}\left(\frac{m_B V_m}{M_B S}\right)^2 \left(\frac{\Delta E_s}{\Delta E_\tau}\right)^2$$

where τ is the time of the galvanostatic injection, m_B is the active material weight, M_B is the molar weight, V_m is the molar volume, S is the electrode surface area, ΔE_s is the charge of open circuit potential (OCP) value between two subsequent charge injection steps, and ΔE_τ is the potential change during the galvanostatic charge injection. As shown in **Figure 12**, a concentration dependence of the Li diffusion coefficient is observed which is characteristic of many intercalation compounds.[36] Furthermore, Li diffusion can be separated into two regions suggesting two different host sites with 0.61 and 0.53 Li. According to the number of lithium accommodated, the first and second region can be assigned to the diffusion of lithium in the interlayer and titanium vacancies, respectively. The first and second region display an average diffusion coefficient of ~5.6.10^{-12} and ~2.2.10^{-12} cm^2 s^{-1}.

Such values are higher than those found in anatase nanoparticles (~10^{-16}-10^{-17} cm^2 s^{-1}).[37]

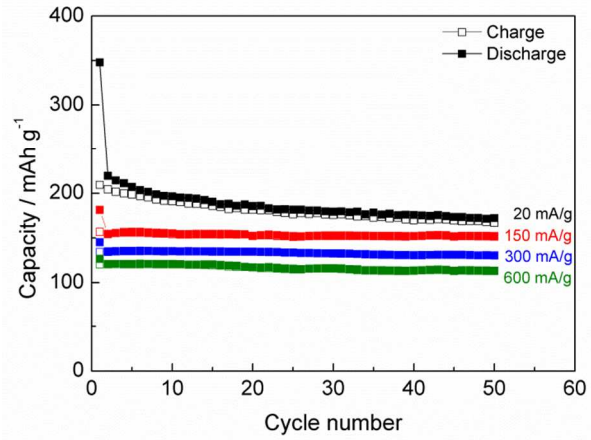

Figure 11. Cycling data obtained for cells cycled against metallic lithium under 20, 150, 300 and 600 mA.g^{-1} within the 1-3 V voltage window using 1M $LiClO_4$ in PC/DME/THF electrolyte.

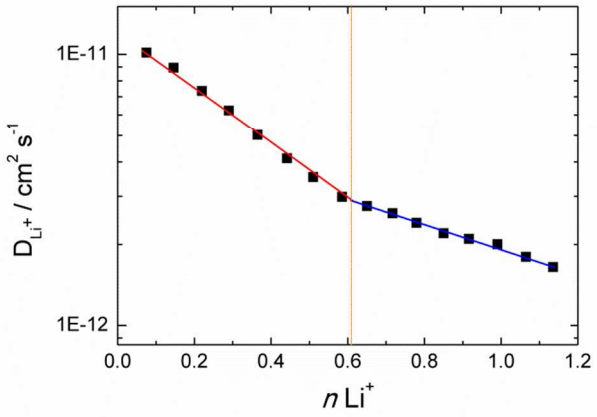

Figure 12. Diffusion coefficient of Li in $Ti_{1.5}\square_{0.5}O_2(OH)_2.0.55H_2O$ as function of number of inserted Li^+.

Intercalation mechanism.

The lithium intercalation mechanism occurring in $Ti_{1.5}\square_{0.5}O_2(OH)_2.0.55H_2O$ was first investigated using high-energy synchrotron-based diffraction measured on electrochemically lithiated (discharged to 1 V) and delithiated (charged to 3 V) electrodes **(Figure S5** in **Supplementary Information)**. Electrochemical lithiation yields to the appearance of broad and weak intensities X-ray peaks indicating an increase of the atomic range-ordering. Moreover, a peak centered at 9.2° (2θ) characteristic of the lepidocrocite type structure[27] confirms that lithium insertion occurs via a solid solution mechanism. After the charge, this peak is still present which confirms the solid-solution mechanism. Moreover, upon delithiation, the x-ray peaks broaden indicating a decrease of the atomic range-ordering. The stability of the lepidocrocite framework upon lithium intercalation/de-intercalation reactions suggests that structural water molecules are maintained within the interlayer.

In the structure of $Ti_{1.5}\square_{0.5}O_2(OH)_2.0.55H_2O$, while as demonstrated by DFT calculations, the large content of titanium vacancies likely contributes to the absence of long-range order, it can also act as host sites for lithium ions.[38] Moreover, Sasaki et *al.*[39] showed that in the lepidocrocite structure, lithium can be accommodated in the octahedral site of the titanium vacancies as well as in trigonal prismatic sites located in the interlayer occupied alternatively by Li ions and H_2O molecules. The filling of both sites likely contributes to the observed increase of the atomic long-range order. Moreover, based on the reversible uptake of around 1.15 Li^+ per formula unit, it can be assumed that the titanium vacancies accommodate up to 0.5 Li^+ and that 0.65 Li^+ ions are inserted in the interlayer sites leading to $[Ti_{1.5}Li_{0.5}]^{4h}O_2(OH)_2.[(H_2O)_{0.55}Li_{0.65}]^{4i}$, where 4h and 4i refers to Wyckoff sites.[27]

Deeper insights into the lithium intercalation mechanism was carried out by probing the local environments of lithium of chemically lithiated compounds using ^{7}Li solid state NMR spectroscopy. $Ti_{1.5}\square_{0.5}O_2(OH)_2.0.55H_2O$ was lithiated using different concentrations of n-butyl lithium leading to 0.20, 0.35 and 0.75 moles of Li^+ per formula unit as determined by ICP-AES. Upon treatment, a gradual color change from white to dark grey was noticed which increases with Li concentrations. High-energy synchrotron-based diffraction data **(Figure S6** in **Supplementary Information)** show that in these conditions, lithiated samples maintained their amorphous features. This contrasts with the slight increase of the long-range order observed by the electrochemical route and may be explained by lower lithiation rate.

^{7}Li solid-state NMR spectra of these samples **(Figure 13)** confirm the increasing insertion of lithium when the concentration of n-butyl lithium increases, *i.e.*, the integrated intensity of the signal increases with the lithiation rate. Whereas paramagnetic compounds exhibit lithium resonances shifted over a range of several hundred ppm,[40] due to the Fermi contact interaction, despite containing $3d^1$ titanium(III), lithiated $Ti_{1.5}\square_{0.5}O_2(OH)_2.0.55H_2O$ samples show ^{7}Li NMR resonances inside the normal diamagnetic ^{7}Li shift range (ca. 5 to −5 ppm).[41] They also show longer spin-lattice T_1 relaxation times (~10s) than expected for ^{7}Li in paramagnetic solids. These values are, however, similar to those observed in lithiated anatase.[42-45] Wagemaker *et al.*[43] concluded that conduction, rather than paramagnetism, is the dominant interaction. Delocalized electron density is then also expected in the $Ti_{1.5}\square_{0.5}O_2(OH)_2.0.55H_2O$ lithiated samples. As the reduction level increases, the ^{7}Li signal becomes broadened and shifts slightly in a positive direction. Moreover, the intensity of the spinning sidebands (from the lower to the intermediate rate) increases. Assuming that fast MAS averages the dipolar interactions, the possible origins for the broad lines and the intense spinning sidebands are distributions of quadrupole interactions and chemical shifts due to disordered environments and interactions with electrons in the conduction band. Spectral decompositions of the slightly asymmetric central lines reveal two contributions to the spectra. The chemical shift, the relative intensity and the line width of each contribution have been fitted, including the spinning sideband manifold, keeping the shapes of the contributions constant for each of the samples (**Table 2** and **Figures S7, S8 and S9** in **Supplementary Information**). The broader resonance (line 2), associated with more intense spinning sidebands, was fitted with a Gaussian line shape, and the narrower resonance (line 1) was fitted with a Lorentzian line shape. In this series of samples there is a gradual increase in the line width of the line 1 while the line width of the line 2 remains essentially invariant. These spectral decompositions show the presence of two discrete sites for intercalated lithium. The Li content in each site increases linearly with the Li content in the sample, in the range 0.20-0.75 (**Table 2** and **Figure S10** in **Supplementary Information**). Based on these Li contents in each site, the lines 1 and 2 are assigned to lithium in the interlayer sites and in the titanium vacancies, respectively. These assignments agree with a higher occupation of the interlayers. The observed broader line 2 and its intense spinning sidebands most likely originate from local structural distortion in the titanate layers due to the occupation in the cationic sites by titanium, lithium and vacancies and in the anionic sites by oxide and hydroxide. Interactions with electrons in the conduction band contribute slightly to the observed line width which remains approximately invariant with the reduction level.

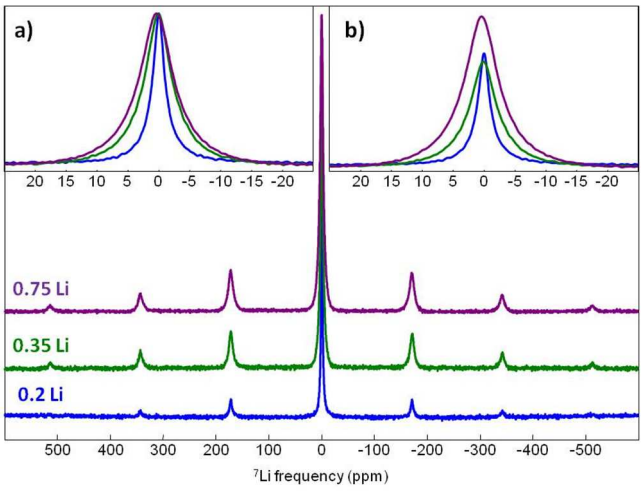

Figure 13. Normalized ^{7}Li MAS (20 kHz) NMR spectra of the chemically lithiated $Ti_{1.5}\square_{0.5}O_2(OH)_2.0.55H_2O$ samples. The moles of Li^+ per formula unit are indicated. Expansions of the central lines are shown in the insets : a) normalized spectra, b) non normalized spectra.

Table 2. Li content (moles of Li^+ per formula unit), isotropic chemical shifts (δ_{iso}, ppm), line widths (LW, ppm) and relative intensities (I, %) of the NMR resonances used for the fit of the ^{7}Li MAS (20 kHz) NMR spectra of chemically lithiated $Ti_{1.5}\square_{0.5}O_2(OH)_2.0.55H_2O$ samples and corresponding Li content (moles of Li^+ per formula unit) in each site. The equations of the linear regressions of the Li content in each site versus the Li content in the sample are $y_1 = 0.567\ x + 0.02$ and $y_2 = 0.434\ x - 0.02$ for lines 1 and 2, respectively.

Li content	Line	δ_{iso}	LW	I	Li content
0.20	1	0.00	2.4	65.6	0.131
	2	-0.20	14.1	34.4	0.069
0.35	1	0.12	4.6	63.1	0.221
	2	0.34	12.1	36.9	0.129
0.75	1	0.36	5.7	59.2	0.444
	2	0.72	13.6	40.8	0.306

In the lepidocrocite structure, the lithium can diffused from one interlayer to the other through titanium vacancies. By using DFT calculations, we monitored the insertion energies of lithium ions for 16 positions along a path that begins in the water interlayer on one side of the titanate layer, passes through the titanium vacancy and ends in the interlayer opposite to the titanate layer. At each position, the geometry of the system was allowed to relax to identify a local energetic minimum. The relaxation of the structure allows for the reorientation of the water molecules as well as deformation around the vacancy. The formation energy for each position of the intercalated ion is calculated as $E_f = E(Li^+|Ti_{63}\square_1(OH)_4O_{124}\cdot 32H_2O) - E(Ti_{63}\square_1(OH)_4O_{124}\cdot 32H_2O) - E(Li^+)$ where the first two terms are the total energy of the system with and without the lithium ion, respectively. **Figure 14a** shows these energies relative to the initial structure where the lithium ion is in the first water interlayer. In systems with a low density of titanium vacancies such as the system investigated here, we observe that the lithium ion experiences two different environments in each interlayer. The interlayer opposite to the vacancy (**Figure 14b**) is roughly 0.1 eV lower in energy than the lithium ion adjacent to the titanium vacancy (**Figure 14c**). In each environment, the ion is three-fold coordinated in a planar geometry by the neighbouring water molecules with Li-O interatomic distances ranging from 1.88 to 1.97 Å. Moreover, we observe that a significantly greater amount of hydrogen bonding between the water molecules and the titanate layer is present when the ion is not adjacent to the titanium vacancy. We hypothesize that it is the additional hydrogen bonding of the surface hydroxyl groups, visible in **Figure 14c** oriented towards the water interlayer that disrupts the hydrogen bonding in the vicinity of the vacancy and thus leads to the slightly higher energy of the system. As the lithium ion passes through the vacancy itself, it becomes four-fold coordinated to two oxygen atoms in the second oxygen layer and the oxygens from the two hydroxyl groups at the surface (**Figure 14d**). **Figure 14d** also shows two slightly longer bonds (2.37Å and 2.52Å) between the ion and two oxygen atoms that lie below the vacancy and towards the center of layer. This coordination of the ion generates a shallow energetic well (~0.2 eV) in which the lithium ion can remain metastable (**Figure 14a**).

In systems with a low density of titanium vacancies, lithium ions energetically prefer the interlayers rather than the vacancies, however in the case that an ion moves into the titanium vacancy, it can become coordinated in a local energy minimum. This coordination within the titanate structure can thus slow ion diffusion. However, the diffusion of the solvated ions within the interlayers is more suited for molecular dynamics simulations, and therefore beyond the reach of the DFT calculations presented here. The observed filling of the titanium vacancy and effective water solvation of lithium ion in the interlayer is in good agreement with the observed ^{7}Li NMR resonances induced by chemical lithiation. We thus confirm the experimental evidence that the lithium storage mechanism implies interlayer and titanium vacancies. It should be noted that the presence of structural water in electrode materials was shown to enable excellent performance in rate capability and cycle life.[46] Our work shows that water molecules contribute to the electrochemical reactions by stabilizing inserted lithium ions. A detailed description on how the desolvation process occurs during the lithium de-intercalation is still needed and can be obtained using further molecular dynamics simulations.

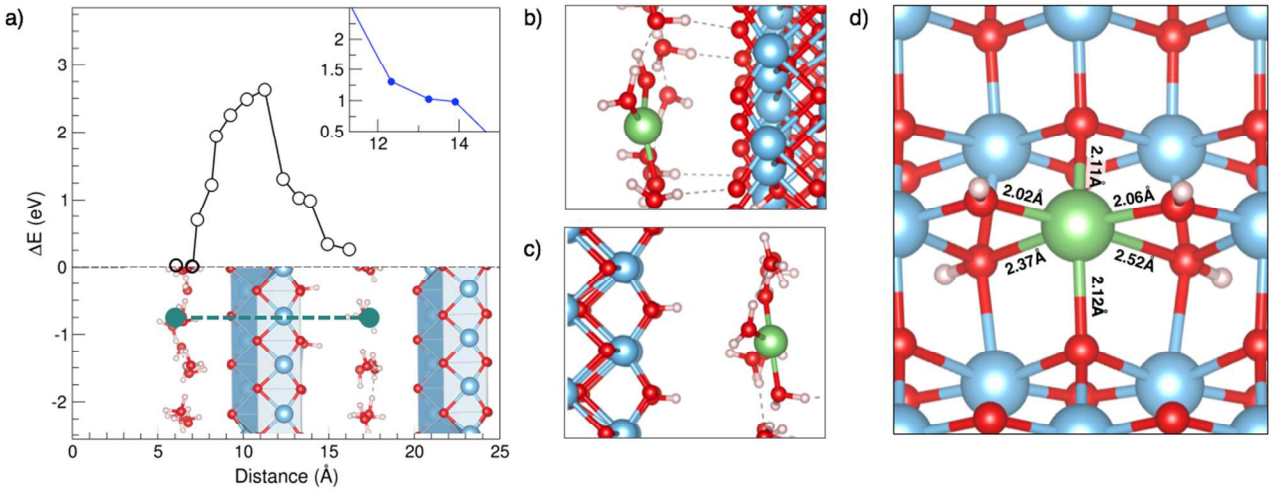

Figure 14. a) The change in total energy calculated based on the position of a lithium ion traveling between one water interlayer to the other via a titanum vacancy. The relaxed geometry shown for the interlayer opposite to the titanium vacancy (b), in the interlayer adjacent to the titanium vacancy (c), and the lithium ion in the titantium vacancy (d).

CONCLUSION

We have revisited the sol-gel chemistry of titanium oxide and found that the crystallization path of anatase TiO_2 implied an intermediate phase featuring a local-range order similar to the layered-type structure of the lepidocrocite as revealed by PDF refinement, ^{1}H solid-state NMR and DFT calculations. This compound has an oxy-hydroxide hydrate composition with a general chemical formula $Ti_{2-x}\square_xO_{4-4x}(OH)_{4x}.nH_2O$, where the substitution of oxide by hydroxide anions leads to the formation of a titanium vacancy ($\square$) and *n* corresponds to interlayer H_2O molecules. ^{1}H MAS NMR enabled to characterize three main hydroxide environments that are Ti$\square$-OH, $Ti_2\square_2$-OH and $Ti_3\square$-OH and layered H_2O molecules.

The synthesis temperature is key to stabilize this phase as a slight increase induces the crystallization of anatase. The phase transition from the lepidocrocite to anatase implies the loss of structural H_2O molecules inducing a condensation of the layers with subsequent structural re-arrangements to form anatase.

When used as an electrode material in lithium batteries, $Ti_{1.5}\square_{0.5}O_2(OH)_2.0.55H_2O$ inserts lithium at an average potential of 1.55 V via a solid-solution behavior implying titanium vacancies and interlayers as host sites. DFT calculations show that within the interlayer, lithium is three-fold coordinated to water while it is four-fold coordinated by two oxygens and two OH groups when sitting in a titanium vacancy. ^{7}Li solid-state NMR confirms the occurrence of the two host sites. The reversible capacity can exceed those of the benchmark electrode LTO with values higher than 200 $mAh.g^{-1}$. With an overall low cost, easy process and an absence of lithium in the composition, this compound is a potential candidate as an anode for batteries.

ASSOCIATED CONTENT

Supporting Information. Additional information is available free of charge via the Internet at http://pubs.acs.org.

AUTHOR INFORMATION

Corresponding Author

*Email: jiwei.ma@upmc.fr (JM); damien.dambournet@upmc.fr (DD)

Notes

The authors declare no competing financial interests.

ACKNOWLEDGMENT

The research leading to these results has received funding from the French National Research Agency under Idex@Sorbonne University for the Future Investments program (No. ANR-11-IDEX-0004-02). This research used resources of the Advanced Photon Source, a U.S. Department of Energy (DOE) Office of Science User Facility operated for the DOE Office of Science by Argonne National Laboratory under Contract No. DE-AC02-06CH11357.

REFERENCES

(1) Dunn, B.; Kamath, H.; Tarascon, J.-M.; Electrical Energy Storage for the Grid: A Battery of Choices, *Science* **2011**, *334*, 928-935.

(2) Larcher, D.; Tarascon, J. M.; Towards greener and more sustainable batteries for electrical energy storage, *Nat. Chem.* **2015**, *7*, 19-29.

(3) Zaghib, K.; Song, X.; Guerfi, A.; Rioux, R.; Kinoshita, K.; Purification process of natural graphite as anode for Li-ion batteries: chemical versus thermal, *J. Power Sources* **2003**, *119–121*, 8-15.

(4) Chen, Z.; Belharouak, I.; Sun, Y. K.; Amine, K.; Titanium-Based Anode Materials for Safe Lithium-Ion Batteries, *Adv. Funct. Mater.* **2013**, *23*, 959-969.

(5) Whittingham, M. S.; Dines, M. B.; n-Butyllithium—An Effective, General Cathode Screening Agent, *J. Electrochem. Soc.* **1977**, *124*, 1387-1388.

(6) Chupas, P. J.; Qiu, X.; Hanson, J. C.; Lee, P. L.; Grey, C. P.; Billinge, S. J. L.; Rapid-acquisition pair distribution function (RA-PDF) analysis, *J. Appl. Crystallogr.* **2003**, *36*, 1342-1347.

(7) Chupas, P. J.; Chapman, K. W.; Lee, P. L.; Applications of an amorphous silicon-based area detector for high-resolution, high-sensitivity and fast time-resolved pair distribution function measurements, *J. Appl. Crystallogr.* **2007**, *40*, 463-470.

(8) Hammersley, A. P.; Svensson, S. O.; Hanfland, M.; Fitch, A. N.; Hausermann, D.; Two-dimensional detector software: From real detector to idealised image or two-theta scan, *High Pressure Res.* **1996**, *14*, 235-248.

(9) Qiu, X.; Thompson, J. W.; Billinge, S. J. L.; PDFgetX2: a GUI-driven program to obtain the pair distribution function from X-ray powder diffraction data, *J. Appl. Crystallogr.* **2004**, *37*, 678.

(10) Farrow, C. L.; Juhas, P.; Liu, J. W.; Bryndin, D.; Božin, E. S.; Bloch, J.; Th, P.; Billinge, S. J. L.; PDFfit2 and PDFgui: computer programs for studying nanostructure in crystals, *J. Phys. Condens. Matter.* **2007**, *19*, 335219-335226.

(11) Massiot, D.; Fayon, F.; Capron, M.; King, I.; Le Calvé, S.; Alonso, B.; Durand, J.-O.; Bujoli, B.; Gan, Z.; Hoatson, G.; Modelling one- and two-dimensional solid-state NMR spectra, *Magn. Reson. Chem.* **2002**, *40*, 70-76.
(12) Hutter, J.; Iannuzzi, M.; Schiffmann, F.; VandeVondele, J.; cp2k: atomistic simulations of condensed matter systems, *WIREs Comput. Mol. Sci.* **2014**, *4*, 15-25.
(13) Perdew, J. P.; Burke, K.; Ernzerhof, M.; Generalized Gradient Approximation Made Simple, *Phys. Rev. Lett.* **1996**, *77*, 3865-3868.
(14) Goedecker, S.; Teter, M.; Hutter, J.; Separable dual-space Gaussian pseudopotentials, *Phys. Rev. B* **1996**, *54*, 1703-1710.
(15) VandeVondele, J.; Krack, M.; Mohamed, F.; Parrinello, M.; Chassaing, T.; Hutter, J.; Quickstep: Fast and accurate density functional calculations using a mixed Gaussian and plane waves approach, *Comput. Phys. Commun.* **2005**, *167*, 103-128.
(16) Yuan, H.; Besselink, R.; Liao, Z.; ten Elshof, J. E.; The swelling transition of lepidocrocite-type protonated layered titanates into anatase under hydrothermal treatment, *Sci. Rep.* **2014**, *4*, 4584.
(17) Liu, G.; Yang, H. G.; Pan, J.; Yang, Y. Q.; Lu, G. Q.; Cheng, H.-M.; Titanium Dioxide Crystals with Tailored Facets, *Chem. Rev.* **2014**, *114*, 9559-9612.
(18) Yu, J.; Dai, G.; Xiang, Q.; Jaroniec, M.; Fabrication and enhanced visible-light photocatalytic activity of carbon self-doped TiO_2 sheets with exposed {001} facets, *J. Mater. Chem.* **2011**, *21*, 1049-1057.
(19) Yang, H. G.; Sun, C. H.; Qiao, S. Z.; Zou, J.; Liu, G.; Smith, S. C.; Cheng, H. M.; Lu, G. Q.; Anatase TiO_2 single crystals with a large percentage of reactive facets, *Nature* **2008**, *453*, 638-641.
(20) Zhang, H.; Chen, B.; Banfield, J. F.; Waychunas, G. A.; Atomic structure of nanometer-sized amorphous TiO_2, *Phys. Rev. B* **2008**, *78*, 214106.
(21) Fernández-García, M.; Belver, C.; Hanson, J. C.; Wang, X.; Rodriguez, J. A.; Anatase-TiO_2 Nanomaterials: Analysis of Key Parameters Controlling Crystallization, *J. Am. Chem. Soc.* **2007**, *129*, 13604-13612.
(22) Borghols, W. J. H.; Lützenkirchen-Hecht, D.; Haake, U.; Chan, W.; Lafont, U.; Kelder, E. M.; van Eck, E. R. H.; Kentgens, A. P. M.; Mulder, F. M.; Wagemaker, M.; Lithium Storage in Amorphous TiO_2 Nanoparticles, *J. Electrochem. Soc.* **2010**, *157*, A582-A588.
(23) Mi, J.-L.; Jensen, K. M. O.; Tyrsted, C.; Bremholm, M.; Iversen, B. B.; In situ total X-ray scattering study of the formation mechanism and structural defects in anatase TiO_2 nanoparticles under hydrothermal conditions, *CrystEngComm* **2015**, *17*, 6868-6877.
(24) Gateshki, M.; Yin, S.; Ren, Y.; Petkov, V.; Titania Polymorphs by Soft Chemistry: Is There a Common Structural Pattern?, *Chem. Mater.* **2007**, *19*, 2512-2518.
(25) Chapman, K. W.; Emerging operando and x-ray pair distribution function methods for energy materials development, *MRS Bull.* **2016**, *41*, 231-240.
(26) Orzali, T.; Casarin, M.; Granozzi, G.; Sambi, M.; Vittadini, A.; Bottom-Up Assembly of Single-Domain Titania Nanosheets on (1x2)-Pt(110), *Phys. Rev. Lett.* **2006**, *97*, 156101.
(27) Sasaki, T.; Watanabe, M.; Michiue, Y.; Komatsu, Y.; Izumi, F.; Takenouchi, S.; Preparation and Acid-Base Properties of a Protonated Titanate with the Lepidocrocite-like Layer Structure, *Chem. Mater.* **1995**, *7*, 1001-1007.
(28) Crocker, M.; Herold, R. H. M.; Wilson, A. E.; Mackay, M.; Emeis, C. A.; Hoogendoorn, A. M.; ^{1}H NMR spectroscopy of titania. Chemical shift assignments for hydroxy groups in crystalline and amorphous forms of TiO_2, *J. Chem. Soc. Faraday Trans.* **1996**, *92*, 2791-2798.
(29) Li, W.; Body, M.; Legein, C.; Dambournet, D.; Identify OH groups in $TiOF_2$ and their impact on the lithium intercalation properties, *J. Solid State Chem.* **2017**, *246*, 113-118.
(30) Li, W.; Body, M.; Legein, C.; Borkiewicz, O. J.; Dambournet, D.; Solvothermal Temperature Drives Morphological and Compositional Changes through Dehydroxyfluorination in Anatase Nanoparticles, *Eur. J. Inorg. Chem.* **2017**, *2017*, 192-197.
(31) Grey, I. E.; Wilson, N. C.; Titanium vacancy defects in sol–gel prepared anatase, *J. Solid State Chem.* **2007**, *180*, 670-678.
(32) Ewing, F. J.; The Crystal Structure of Lepidocrocite, *J. Chem. Phys.* **1935**, *3*, 420-424.
(33) Augustyn, V.; Simon, P.; Dunn, B.; Pseudocapacitive oxide materials for high-rate electrochemical energy storage, *Energy Environ. Sci.* **2014**, *7*, 1597-1614.
(34) Levy, S. C.; Bro, P. *Battery Hazards and Accident Prevention*; Springer, 1994.
(35) Fattakhova, D.; Kavan, L.; Krtil, P.; Lithium insertion into titanium dioxide (anatase) electrodes: microstructure and electrolyte effects, *J. Solid State Electrochem.* **2001**, *5*, 196-204.
(36) Van der Ven, A.; Bhattacharya, J.; Belak, A. A.; Understanding Li Diffusion in Li-Intercalation Compounds, *Acc. Chem. Res.* **2013**, *46*, 1216-1225.
(37) Wang, J.; Polleux, J.; Lim, J.; Dunn, B.; Pseudocapacitive Contributions to Electrochemical Energy Storage in TiO_2 (Anatase) Nanoparticles, *J. Phys. Chem. C* **2007**, *111*, 14925-14931.
(38) Hahn, B. P.; Long, J. W.; Rolison, D. R.; Something from Nothing: Enhancing Electrochemical Charge Storage with Cation Vacancies, *Acc. Chem. Res.* **2013**, *46*, 1181-1191.
(39) Sasaki, T.; Kooli, F.; Iida, M.; Michiue, Y.; Takenouchi, S.; Yajima, Y.; Izumi, F.; Chakoumakos, B. C.; Watanabe, M.; A Mixed Alkali Metal Titanate with the Lepidocrocite-like Layered Structure. Preparation, Crystal Structure, Protonic Form, and Acid−Base Intercalation Properties, *Chem. Mater.* **1998**, *10*, 4123-4128.
(40) Messinger, R. J.; Ménétrier, M.; Salager, E.; Boulineau, A.; Duttine, M.; Carlier, D.; Ateba Mba, J.-M.; Croguennec, L.; Masquelier, C.; Massiot, D.; Deschamps, M.; Revealing Defects in Crystalline Lithium-Ion Battery Electrodes by Solid-State NMR: Applications to $LiVPO_4F$, *Chem. Mater.* **2015**, *27*, 5212-5221.
(41) Günther, H. *Lithium NMR in Encyclopedia of Nuclear Magnetic Resonance*; John Wiley & Sons, Ltd: Chichester, 2007.
(42) Luca, V.; Hanley, T. L.; Roberts, N. K.; Howe, R. F.; NMR and X-ray Absorption Study of Lithium Intercalation in Micro- and Nanocrystalline Anatase, *Chem. Mater.* **1999**, *11*, 2089-2102.
(43) Wagemaker, M.; van de Krol, R.; Kentgens, A. P. M.; van Well, A. A.; Mulder, F. M.; Two Phase Morphology Limits Lithium Diffusion in TiO_2 (Anatase): A ^{7}Li MAS NMR Study, *J. Am. Chem. Soc.* **2001**, *123*, 11454-11461.
(44) Lo, A. Y. H.; Schurko, R. W.; Vettraino, M.; Skadtchenko, B. O.; Trudeau, M.; Antonelli, D. M.; Solid-State ^{23}Na and ^{7}Li NMR Investigations of Sodium- and Lithium-Reduced Mesoporous Titanium Oxides, *Inorg. Chem.* **2006**, *45*, 1828-1838.
(45) Bottke, P.; Ren, Y.; Hanzu, I.; Bruce, P. G.; Wilkening, M.; Li ion dynamics in TiO_2 anode materials with an ordered hierarchical pore structure - insights from ex situ NMR, *Phys. Chem. Chem. Phys.* **2014**, *16*, 1894-1901.
(46) Nam, K. W.; Kim, S.; Yang, E.; Jung, Y.; Levi, E.; Aurbach, D.; Choi, J. W.; Critical Role of Crystal Water for a Layered Cathode Material in Sodium Ion Batteries, *Chem. Mater.* **2015**, *27*, 3721-3725.

TOC